

# Microstructure Modification of Liquid Phase Sintered Fe–Ni–B–C Alloys for Improved Mechanical Properties



JINSU YOU, HYOUNG GYUN KIM, JONGWON LEE, KU KANG, HYUCK MO LEE, MIYOUNG KIM, and SEONG-HYEON HONG

Powder metallurgy (P/M) has been widely used in automobile, home appliances, and electronic devices, but its uses are very limited due to the low relative density of 85 to 95 pct. The Fe–Ni–B–C alloy system can mitigate the aforementioned issues by the liquid phase sintering, which results in a nearly full densification. However, the boron-containing alloys produced the brittle eutectic phases [Fe<sub>3</sub>(C, B) and Fe<sub>2</sub>B] along the grain boundaries, which are detrimental to the mechanical properties. The main objective of this study is to improve the ductility of boron-containing alloys through the microstructure modification. For this, the volume fraction of solidified phase was optimized by controlling the composition, and the coarsening of solidified  $\alpha$ -Fe particles into the pearlite matrix was induced by a post annealing, which reduces the continuous network of eutectic phases and increased the grain continuity. In addition, the effect of microstructure modification on the mechanical properties of Fe–B–C and Fe–Ni–B–C alloys was comparatively investigated. As a result of microstructure modification, the post-annealed Fe–1Ni–0.4B–0.8C alloy exhibited a high elongation to failure of 5.2 pct.

<https://doi.org/10.1007/s11661-021-06392-5>

© The Minerals, Metals & Materials Society and ASM International 2021

## I. INTRODUCTION

**POWDER** metallurgy (P/M) is an efficient process for manufacturing the mechanical parts of high quality and accuracy at low cost.<sup>[1]</sup> However, the use of conventionally sintered products is limited due to their low relative density of 85 to 95 pct.<sup>[2]</sup> Liquid phase sintering (LPS) is a consolidation process of powder compacts at the temperature above the solidus of more than one component, that is, in the presence of wetting liquid phase. The densification is achieved *via* particle rearrangement, solution-precipitation, and coarsening and grain growth during sintering.<sup>[3,4]</sup> The appropriate amount of liquid phase during LPS is known to be 5 to 15 vol pct.<sup>[4,5]</sup> Among the various alloying elements for LPS,<sup>[6–8]</sup> boron (B) has all the features of an effective sintering enhancer for ferrous systems with high hardenability and mechanical properties, resulting from the

eutectic reaction ( $\gamma$ -Fe + Fe<sub>2</sub>B  $\rightarrow$  L).<sup>[9–13]</sup> Carbon (C) is an indispensable element for P/M alloy steels due to its low cost and high mechanical properties,<sup>[14,15]</sup> and also facilitates the LPS densification by lowering the temperature of liquid formation.<sup>[16–18]</sup> Moreover, several attempts have been made to further improve the densification and mechanical properties of boron-containing alloys through the addition of alloying elements such as Mo, Cu, Cr, Al, and Mn.<sup>[19–23]</sup> Among them, nickel (Ni) is an important element for Fe-based alloys due to its high strength, hardenability, and solid solution strengthening.<sup>[24–26]</sup> Several studies have reported that the Ni addition to the Fe–B system accelerated the boron diffusion in  $\gamma$ -Fe similar to carbon and decreased the temperature for eutectic reaction and thus, improved the densification of boron-containing alloys.<sup>[27–30]</sup> In addition, Wu *et al.* found that the Ni addition to the Fe–Mo–B–C steels lowered the temperature of eutectic reaction, resulting in the microstructural change from Fe<sub>2</sub>B and Fe<sub>3</sub>(C, B) to M<sub>3</sub>(C, B) (Ni ~ 0.8 at. pct).<sup>[31,32]</sup> Likewise, the addition of the appropriate alloying elements was beneficial to the densification of boron-containing alloys; however, the improvement of elongation property was very limited because a large amount of liquid phase produced the continuous network of eutectic hard phases [M<sub>23</sub>B<sub>6</sub>, M<sub>3</sub>(C, B), and M<sub>2</sub>B] at the grain boundaries.<sup>[33,34]</sup>

JINSU YOU, HYOUNG GYUN KIM, JONGWON LEE, MIYOUNG KIM and SEONG-HYEON HONG are with the Department of Materials Science and Engineering and Research Institute of Advanced Materials (RIAM), Seoul National University, Seoul 08826, Republic of Korea. Contact e-mail: shhong@snu.ac.kr KU KANG and HYUCK MO LEE are with the Department of Materials Science and Engineering, Korea Advanced Institute of Science and Technology (KAIST), Taejeon 34141, Republic of Korea.

Manuscript submitted December 22, 2020; accepted July 8, 2021.

Article published online July 21, 2021

Recently, the mechanical properties of liquid phase sintered alloys have been studied based on the microstructural modification, which prevented the continuous network of eutectic phases and increased the grain continuity.<sup>[35–37]</sup> Several studies suggested that the microstructure of boron-containing alloys can be modified by composition<sup>[9,12]</sup> and heat treatment.<sup>[36,38]</sup> Peng *et al.* reported that the amount of boron-carbides remarkably decreased as the boron content decreased.<sup>[10]</sup> Lentz *et al.* found that the volume fraction of the eutectic hard phases [Fe<sub>3</sub>(C, B) and Fe<sub>2</sub>B] decreased by lowering the B/(B + C) ratio of Fe–B–C alloys.<sup>[12]</sup> In addition, Li *et al.* suggested that the heat treatment has the effects on the morphology of hard phase, which obviously prevented the formation of continuous hard phase network.<sup>[38]</sup> Liu *et al.* indicated that the boride network was broken up and changed into isolated distribution after heat treatment.<sup>[36]</sup> It is speculated that the ductile property of Fe–Ni–B–C alloys can be improved through the composition control and heat treatment, which optimize the volume fraction of solidified phases and reduce the continuous network of eutectic phases. However, the effect of microstructure modification on mechanical properties of Fe–Ni–B–C alloys has been rarely investigated.

The objective of the present study was focused on improving the elongation to failure in Fe–B–C ternary alloys. The Ni addition was introduced to promote the eutectic reaction and thus, improve the densification of boron-containing alloys. To reduce the continuous network of hard eutectics, the composition was controlled to achieve the system with the optimized hard phase fraction, and heat treatment was performed to induce the coarsening of solidified  $\alpha$ -Fe particles into the matrix. In addition, the effects of microstructure modification on the mechanical properties of Fe–Ni–B–C alloys were thoroughly investigated. Under the optimized condition, the post-annealed Fe–1Ni–0.4B–0.8C alloy exhibited a significant increase of ductility (elongation to failure).

## II. EXPERIMENTAL

The starting powders used for sintering were commercially available water-atomized iron (< 150  $\mu\text{m}$ , ASC100.29, Hogan), boron [ $\sim 15 \mu\text{m}$  ( $D_{50}$ ), iNexus, Inc.], synthetic graphite (< 20  $\mu\text{m}$ , Sigma-Aldrich), and nickel (< 50  $\mu\text{m}$ , Sigma-Aldrich) powders. The investigated compositions were Fe–0.6B–0.8C, Fe–0.4B–0.8C, Fe–1Ni–0.6B–0.8C and Fe–1Ni–0.4B–0.8C in wt pct. The powder mixture was prepared by hand or V-mixer and compacted into  $\varnothing 10$  mm pellets at a compacting pressure of 600 MPa without a lubricant. All the samples were sintered at 1180  $^{\circ}\text{C}$  for 3 hours in a vacuum ( $10^{-2}$  to  $10^{-3}$  Torr) and furnace-cooled. The water quenching was carried out at a cooling rate of 150  $^{\circ}\text{C}/\text{min}$  and the post annealing was performed at 1000  $^{\circ}\text{C}$  for 0 to 24 hours under a vacuum condition ( $10^{-2}$  to  $10^{-3}$  Torr). The sintered density (apparent density) of Fe–Ni–B–C alloys was determined by Archimedes immersion method. For the microstructure observation, the surface of sintered samples was prepared by

grinding, mechanical polishing with diamond slurry down to 0.25  $\mu\text{m}$ , and then electro-polishing using 10 pct perchloric acid and 90 pct methanol solution for 30 seconds, and investigated by optical microscopy (Nikon L-150, OM), scanning electron microscope (Fe-SEM, SU-70) equipped with electron backscatter diffraction (EBSD) and energy dispersive X-ray spectroscopy (EDS). For transmission electron microscopy (TEM, Tecnai F20, FEI) observation, the cross sectional specimen was prepared by focused ion beam (FIB, Helios Nano Lab450, FEI) technique. The bulk hardness was measured using Rockwell A hardness measurement (Mitutoyo, Japan) on the polished surface, and the nanoindentation was carried out by Hysitron TriboLab 750 Ubi nanoindentation system equipped with a Berkovich indenter. For the tensile test, the specimens were prepared as per MPIF standard 10 and a small amount of lubricant (0.4 wt pct, Kenolube) was used to minimize the friction between pressing die and specimen. The tensile test was carried out using a universal testing machine (Instron 5584) with a strain rate of 1.86 mm/min.

## III. RESULTS AND DISCUSSION

The volume fraction of liquid phase in Fe–B–C and Fe–Ni–B–C alloy systems was calculated with Thermo-Calc<sup>[39]</sup> using a TCFE 2000 thermodynamic database (Figure 1). The Ni addition to Fe–B–C system slightly decreased the liquid phase formation temperature and increased the volume fraction of liquid phase, because Ni contributes to the formation of  $\gamma$ -Fe and promotes the eutectic reaction  $\gamma\text{-Fe} + \text{Fe}_2\text{B} \rightarrow \text{L}$ .<sup>[27–32]</sup> When the B content decreased from 0.6 to 0.4 wt pct at fixed C content of 0.8 wt pct, the volume fraction of liquid phase significantly decreased from 26 to 18 vol pct at 1180  $^{\circ}\text{C}$ . As a result, the apparent density of Fe–0.4B–0.8C alloy (7.65  $\text{g}/\text{cm}^3$ ) was higher than that of Fe–0.6B–0.8C alloy (7.44  $\text{g}/\text{cm}^3$ ) (Figure 2), possibly due to the appropriate amount of liquid phase required for filling the pores in

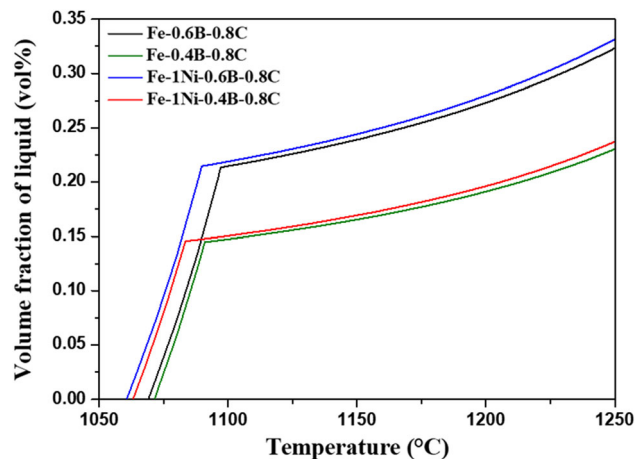


Fig. 1—Volume fraction of liquid phase in Fe–0.6B–0.8C, Fe–0.4B–0.8C, Fe–1Ni–0.6B–0.8C, and Fe–1Ni–0.4B–0.8C alloys as a function of temperature.

green compacts. The relative green density was in the range of 89.7 to 91.1 pct at a compacting pressure of 600 MPa (Figure S-1 refer to Supplementary Materials). In addition, the Ni addition promoted the densification and thus, Fe–Ni–B–C alloys showed the higher apparent density compared to the Fe–B–C alloys. Furthermore, the apparent density of quenched Fe–Ni–B–C alloy had the higher density than that of quenched Fe–B–C alloy, indicating that the Ni-containing liquid phase enhanced the diffusion and promoted the densification at the sintering temperature (Figure S-2). The slightly lower apparent density of quenched alloys compared to the furnace-cooled counterparts can be attributed to the limited diffusion leading to the densification during solidification.

The optical and SEM micrographs of liquid phase sintered Fe–B–C and Fe–Ni–B–C alloys are shown in Figure 3. The Fe–B–C alloys showed the typical liquid phase sintered microstructure consisting of spherical grains (pearlite and re-precipitated ferrite) and  $\alpha$ -Fe

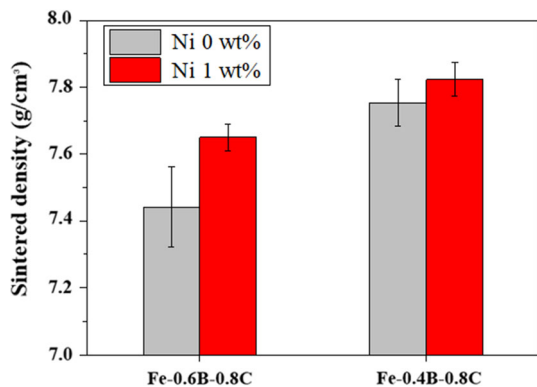


Fig. 2—Apparent density of liquid phase sintered Fe–0.6B–0.8C, Fe–0.4B–0.8C, Fe–1Ni–0.6B–0.8C, and Fe–1Ni–0.4B–0.8C alloys sintered at 1180 °C for 3 hours and furnace-cooled.

particle embedded  $\text{Fe}_3(\text{C}, \text{B})$  continuous network (Figures 3(a) and (b)). The EDS analysis further confirmed the constituent phases and element distribution in the Fe–B–C alloy (Figure S-3). On the other hand, the re-precipitated ferrite was not observed in the Fe–Ni–B–C alloys and the microstructure of Fe–Ni–B–C alloys was composed of pearlite grains and  $\alpha$ -Fe particle embedded  $(\text{Fe}, \text{Ni})_3(\text{C}, \text{B})$  grain boundaries (solidified phases) (Figures 3(c) and (d)). The OM and SEM images also indicated that the decrease of B content in Fe–B–C and Fe–Ni–B–C alloys decreased the extent of agglomeration of solidified phases, resulting in the increase of grain continuity. The point EDS analysis indicated that Ni was relatively homogeneously present at both grains and grain boundaries, and the Ni addition did not change the hard phases ( $\text{Fe}_3\text{C}$  type) and distribution of B and C (Figure S-4).<sup>[31,32]</sup>

The volume fraction of solidified phases in the sintered alloys was determined by electron backscatter diffraction (EBSD, Figure 4). Consistent with the Thermo-Calc results (Figure 1), the decrease of B content from 0.6 to 0.4 wt pct decreased the volume fraction of solidified phases from 15 to 16 to 10, which led to the increase of grain continuity. However, the addition of 1 wt pct Ni did not significantly change the content of solidified phases. To investigate the effect of Ni addition on the microstructure development, the phase change during the solidification of Fe–0.6B–0.8C and Fe–1Ni–0.6B–0.8C alloys was calculated by Thermo-Calc under the equilibrium condition (Figure S-5).<sup>[12,29]</sup> As the temperature was lowered from the sintering temperature, the amount of liquid was rapidly dropped and the liquid was transformed to the solidified phases ( $\text{M}_2\text{B}$  and  $\text{M}_{23}\text{C}_6$ ) along with the progress of the solidification process. Upon the subsequent cooling, phase transformation and diffusion occurred resulting in the pearlite grain ( $\alpha$ -Fe and  $\text{Fe}_3\text{C}$ ) and hard phase ( $\text{Fe}_3(\text{C}, \text{B})$  or  $(\text{Fe}, \text{Ni})_3(\text{C}, \text{B})$ ). The Ni addition to the Fe–B–C system facilitated the eutectic reaction,<sup>[31,32]</sup> and thus, the

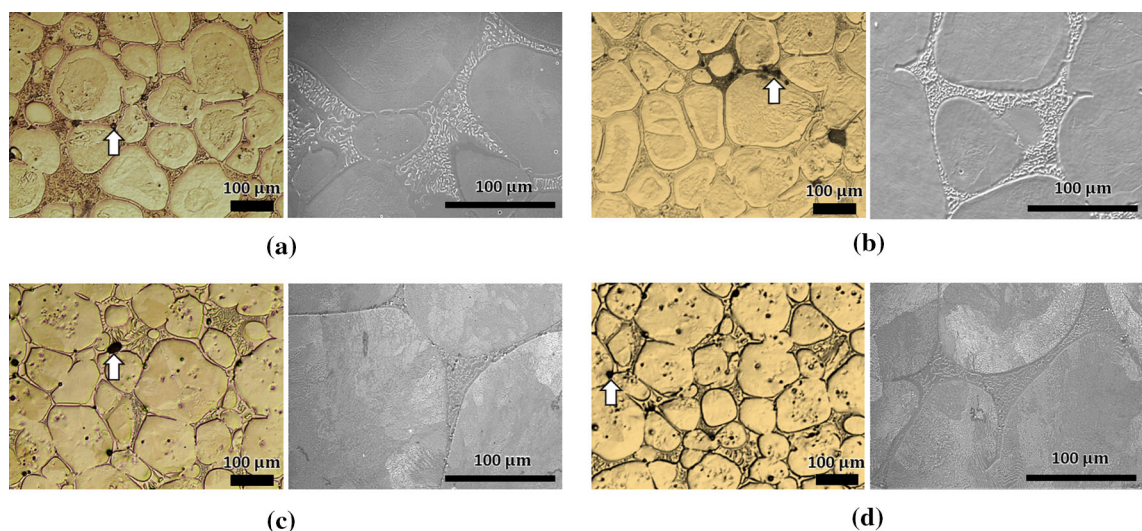


Fig. 3—Optical and SEM micrographs of (a) Fe–0.6B–0.8C, (b) Fe–0.4B–0.8C, (c) Fe–1Ni–0.6B–0.8C, and (d) Fe–1Ni–0.4B–0.8C alloys. The dark spots marked by an arrow are etching trace (or defect).



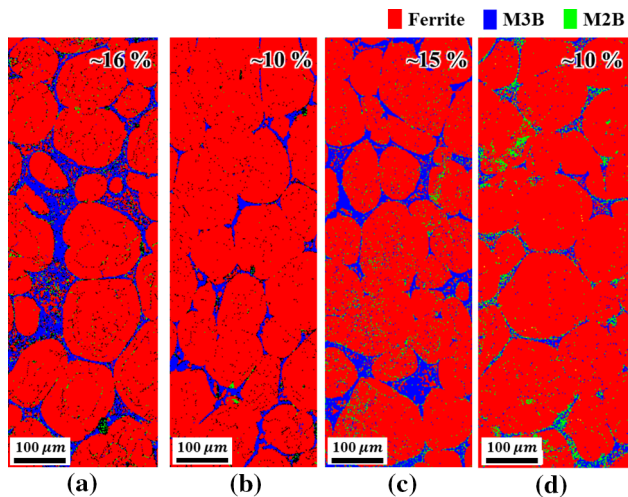


Fig. 4—Phase identification and fraction determined by EBSD in (a) Fe-0.6B-0.8C, (b) Fe-0.4B-0.8C, (c) Fe-1Ni-0.6B-0.8C, and (d) Fe-1Ni-0.4B-0.8C alloys.

fraction of solidified phases ( $M_2B$ ,  $M_{23}C_6$  and  $Fe_3C$ ) increased compared to that in Fe-0.6B-0.8C alloy. In addition, a complete austenite decomposition to ferrite and carbides has been observed at the higher temperature. The microstructure of the Fe-0.6B-0.8C and Fe-1Ni-0.6B-0.8C alloys quenched from 950 °C (below the solidus temperature) was further examined to investigate the effect of Ni addition on the microstructure development (Figure S-6). From this period,  $\gamma$ -Fe particles formed from the liquid were diffused and coalesced into the matrix grain. A large number of  $\gamma$ -Fe particles were observed at the grain boundaries of quenched Fe-0.6B-0.8C alloy (Figure S-6(a)). Upon the subsequent cooling, phase transformation and rearrangement occurred exhibiting the spherical grains composing of pearlite and ferrite in Fe-0.6B-0.8C alloy (Figure 3(a)). On the other hand, most of  $\gamma$ -Fe particles were diffused into Fe matrix before the transformation to pearlite, resulting in the coalesced grains in quenched Fe-1Ni-0.6B-0.8C alloy (Figure S-6(b)). It implied that the Ni addition also facilitated the diffusion of solidified  $\gamma$ -Fe during solidification, which lead to the improved densification (7.44 vs. 7.75 g/cm<sup>3</sup>) and induced the microstructure change from pearlite/re-precipitated ferrite to pearlite.

To examine the effects of composition on the mechanical properties, hardness and tensile tests were carried out on the sintered specimens. Figure 5(a) represents the bulk hardness of Fe-B-C and Fe-Ni-B-C alloys determined by Rockwell A hardness measurement. With Ni addition, the bulk hardness of Fe-Ni-B-C alloys greatly increased from 33.3 to 34.5 to 53.1 to 58.8, which can be attributed to the enhanced density, solid solution strengthening, and microstructural change of grains from pearlite and re-precipitated ferrite to pearlite and of grain boundary from  $Fe_3(C, B)$  to  $(Fe, Ni)_3(C, B)$ . With decreasing the B content, the sintered density increased in both systems, but the bulk hardness of the Fe-Ni-B-C alloy slightly decreased from 58.8 to 53.1, which can be attributed to the

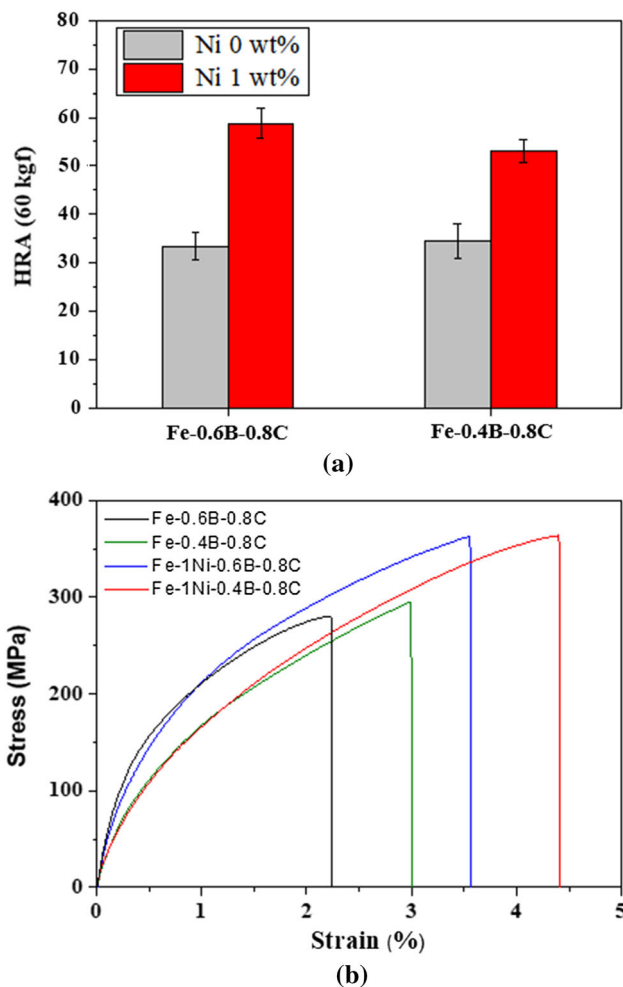


Fig. 5—(a) Bulk hardness and (b) tensile stress-strain curves of Fe-0.6B-0.8C, Fe-0.4B-0.8C, Fe-1Ni-0.6B-0.8C, and Fe-1Ni-0.4B-0.8C alloys.

decrease of the volume fraction of solidified phases from 15 to 16 to 10 pct with decreasing the B content. To compare the hardness of constituent phases, the nanoindentation test was performed on the Fe-0.6B-0.8C and Fe-1Ni-0.6B-0.8C alloys. The hardness was calculated from the load-displacement curve using Oliver-Pharr method.<sup>[40]</sup> With Ni addition, the hardness of grain (pearlite) increased from 2.7 to 3.1 GPa (Figures 6(a) and (c)), and the hardness of grain boundary increased from 13.8 to 16.8 GPa (Figures 6(b) and (d)), which can be attributed to the solid solution strengthening.

The tensile stress-strain curves for Fe-B-C and Fe-Ni-B-C alloys are presented in Figure 5(b). The tensile strength of specimen increased from 280 to 296 to 362 to 363 MPa with Ni addition,<sup>[1,41-44]</sup> which was due to the similar reasons for the improved bulk hardness. The elongation to failure increased from 2.2 to 3.0 to 3.6 to 4.4 pct, which can be attributed to the increased apparent density. Especially, the elongation to failure was greatly improved with decreasing the B content in Fe-B-C and Fe-Ni-B-C alloys. It indicated that the decrease of the volume fraction of solidified phases was

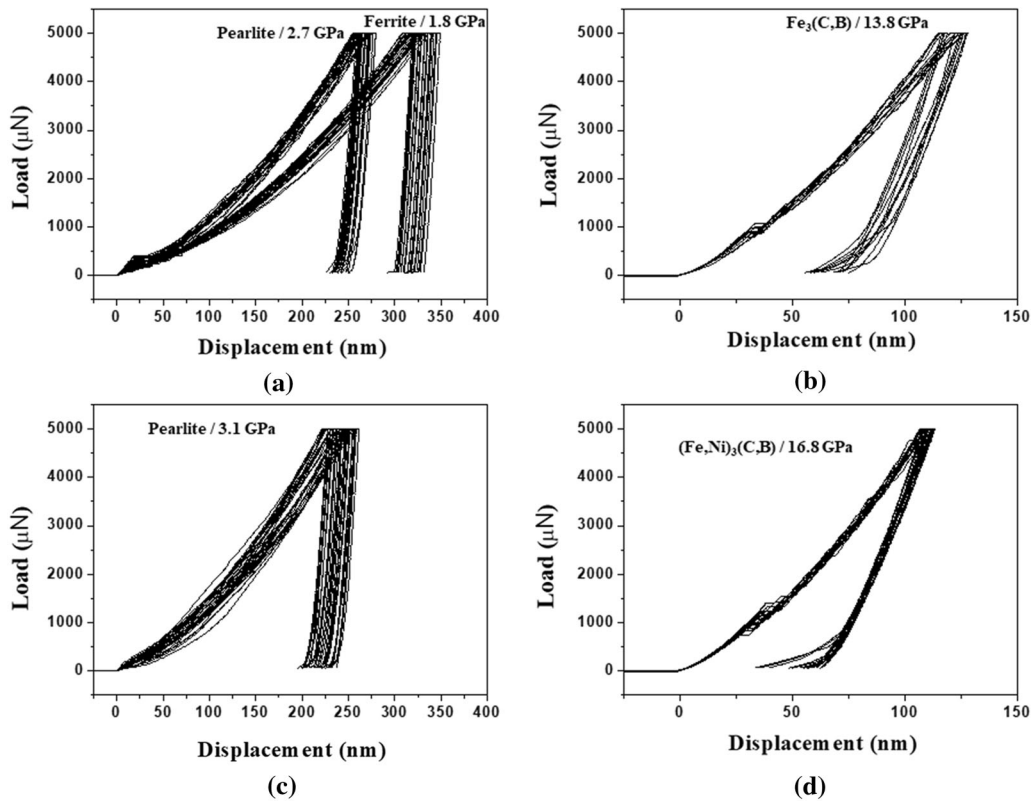


Fig. 6—Nanoindentation load–displacement curves of grain and grain boundary of (a, b) Fe–0.6B–0.8C and (c, d) Fe–1Ni–0.6B–0.8C alloys.

effective to increase the grain continuity and suppress the failure at the grain boundaries during tensile test.<sup>[35–38]</sup> As a result of composition variation, the elongation to failure reached 4.4 pct in Fe–1Ni–0.4B–0.8C alloy, and this value was higher than that of boron-containing alloys,<sup>[41–44]</sup> and even similar to that of solid-state sintered alloys,<sup>[1]</sup> possibly due to the increased density and decrease of the volume fraction of solidified phase.

To further improve the elongation to failure, the quenching and post annealing was carried out in an aim to obtain the desired microstructure through the coarsening of solidified  $\alpha$ -Fe particles to the matrix grains. Figures 7(a) and (b) present the optical and SEM micrographs of Fe–1Ni–0.4B–0.8C alloy after post annealing. The asymmetric quenching process led to the microstructural change of the grain boundaries into the well-dispersed alternated layers of hard phase and  $\alpha$ -Fe (Figure S-7).<sup>[45,46]</sup>

However, during post annealing, the embedded  $\alpha$ -Fe particles started to coarsen and merge into the grains (Figure S-8(a)) and the grain boundary was gradually changed from continuous boride network to discontinuous structure (Figure S-8(b)). After 24 hours post annealing, the Fe–1Ni–0.4B–0.8C alloy exhibited a necklace microstructure such that the pearlite grains were linked with each other and hard phases were isolated at the grain boundaries. To investigate the

constituent phases of post-annealed Fe–1Ni–0.4B–0.8C alloy, the specimen which contained the grains and grain boundaries was prepared by FIB technique as shown in the low magnification TEM image (Figure 7(c)). The selected area electron diffraction (SAED) pattern of the grain area (Spot 1) was indexed to be  $\alpha$ -Fe with a  $[01\bar{2}]$  zone axis (Figure 7(d)) and the hard phase area (Spot 2) was indexed to be  $\text{Fe}_3\text{C}$  with a  $[1\bar{2}0]$  zone axis (Figure 7(e)).<sup>[47]</sup> Based on the microstructure and EDS analysis (Table I), the grain and hard phase were identified to be pearlite and  $(\text{Fe, Ni})_3(\text{C, B})$ , respectively, which were identical to those before the heat treatment. Thus, a significant grain coarsening with an obvious necking was observed after post annealing without the transformation.

Upon quenching and post annealing, the mechanical characteristics (apparent density, bulk hardness and tensile strength) of post-annealed Fe–1Ni–0.4B–0.8C alloy were mostly recovered to their initial values (Figure S-9).<sup>[48]</sup> Especially, the elongation to failure dramatically increased from 2.8 to 5.2 pct (Figure 8), which was even higher than the initial value (4.4 pct). The increase of elongation to failure can be attributed to the increase of grain continuity after the post annealing. This results showed that the microstructure consisting of linked pearlite grains and isolated  $(\text{Fe, Ni})_3(\text{C, B})$  particles was to be highly resistant to failure, improving the elongation of failure in Fe–1Ni–0.4B–0.8C alloys.

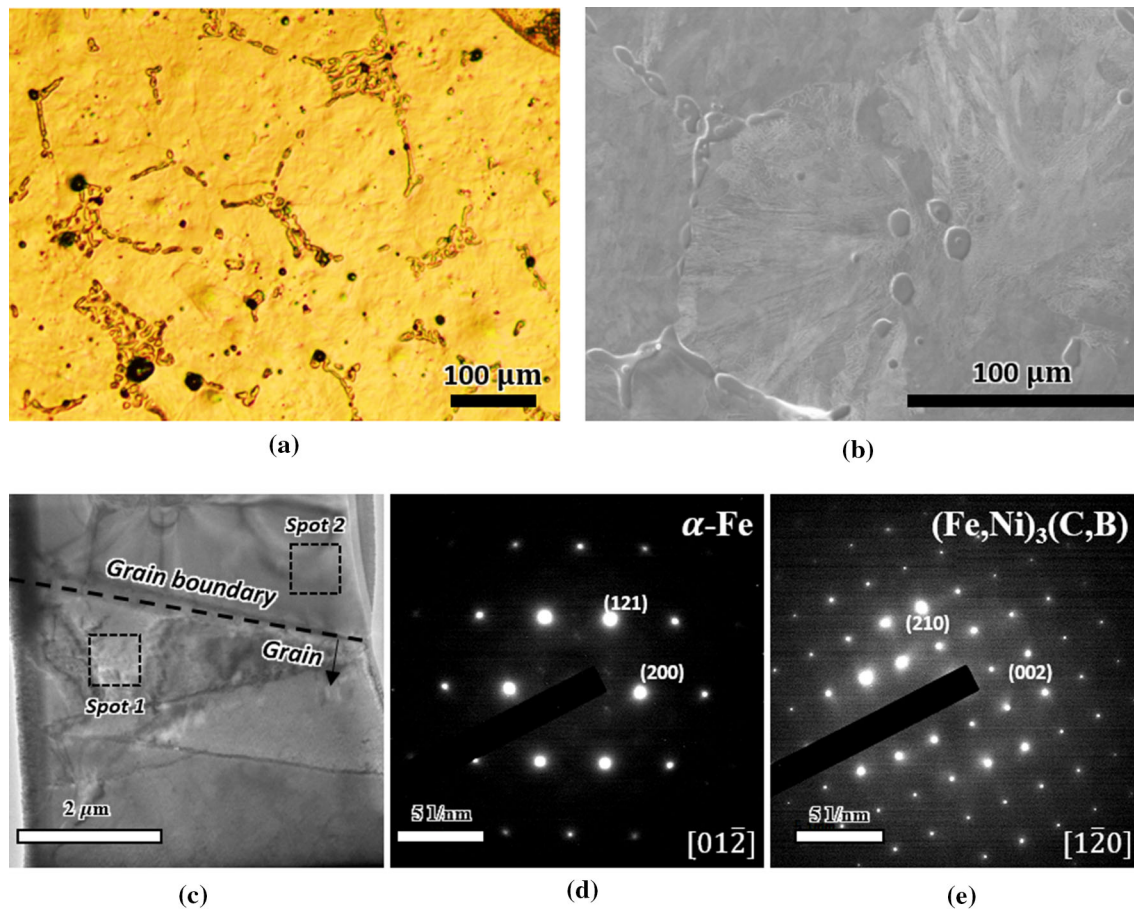


Fig. 7—(a) Optical and (b) SEM micrographs of Fe-1Ni-0.4B-0.8C alloy post-annealed at 1000 °C for 24 hours, (c) low magnification HAADF-STEM image of grain and grain boundary in Fe-1Ni-0.4B-0.8C alloy and selected area diffraction patterns (SADPs) of (d) spot 1 ( $\alpha$ -Fe) and (e) spot 2 ( $(\text{Fe, Ni})_3(\text{C, B})$ ).

Table I. Chemical Composition (Wt Pct) of Selected Areas (Spots 1 and 2) by EDS

Phase	Fe	Ni	B	C
Ferrite (Spot 1)	98.26	1.0	—	0.74
$(\text{Fe, Ni})_3(\text{C, B})$ (Spot 2)	92.91	0.79	2.2	4.1

#### IV. CONCLUSIONS

In this study, Fe-Ni-B-C alloys were successfully fabricated by liquid phase sintering to achieve a high densification. Ni addition was employed to decrease the eutectic temperature and improve the densification and mechanical properties of Fe-B-C alloys. The Ni addition facilitated the diffusion of solidified  $\gamma$ -Fe during solidification, which lead to the improved densification and induced the microstructure change from pearlite/re-precipitated ferrite to pearlite. For the improvement of elongation property, the composition controlling and post annealing were performed to modify the microstructure. The decrease of B content decreased the volume fraction of hard phases, and the post annealing induced the discontinuous grain boundary

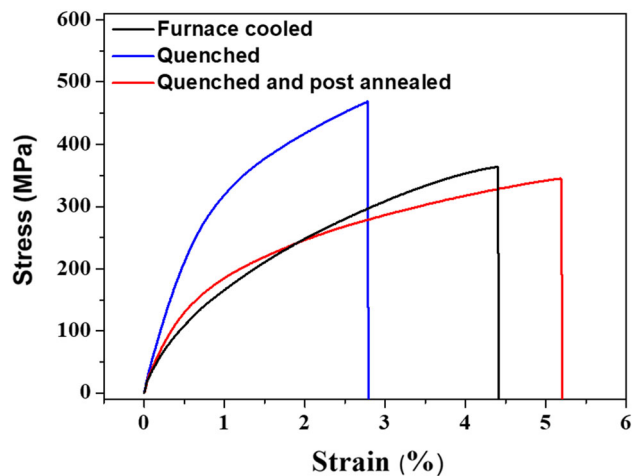


Fig. 8—Stress-strain curves of furnace-cooled, quenched, and post-annealed Fe-1Ni-0.4B-0.8C alloys.

structure composed of the isolated hard phases. A significant improvement on elongation was observed in Fe-Ni-B-C alloy. The increase of elongation to failure can be attributed to the optimized volume fraction of hard phase and the increase of grain continuity, which



suppressed the continuous network of eutectic phases. As a result of microstructure modification, the post-annealed Fe–1Ni–0.4B–0.8C alloy resulted in the high elongation to failure of 5.2 pct.

## ACKNOWLEDGMENTS

This work was supported by the National Research Foundation of Korea (NRF) Grant funded by the Korea government (MSIT) (No. NRF-2020 R1A5A6017701).

## SUPPLEMENTARY INFORMATION

The online version contains supplementary material available at <https://doi.org/10.1007/s11661-021-06392-5>.

## REFERENCES

1. K.S. Narasimhan: *Mater. Chem. Phys.*, 2001, vol. 67, pp. 56–65.
2. A. Hadrboletz and B. Weiss: *Int. Mater. Rev.*, 1997, vol. 42, pp. 1–44.
3. B.A. James: *Powder Metall.*, 1985, vol. 28, pp. 121–30.
4. R.M. German, P. Suri, and S.J. Park: *J. Mater. Sci.*, 2009, vol. 44, pp. 1–39.
5. J. Liu, A. Upadhyaya, and R.M. German: *Metall. Mater. Trans. A*, 1999, vol. 30A, pp. 2209–20.
6. H. Borgström and L. Nyborg: *J. Iron Steel Res. Int.*, 2007, vol. 14, pp. 70–76.
7. H. Preusse and J.D. Bolton: *Powder Metall.*, 1999, vol. 42, pp. 51–62.
8. S.J. Jamil and G.A. Chadwick: *Powder Metall.*, 1985, vol. 28, pp. 65–71.
9. M. Marucci, A. Lawley, R. Causton, and S. Saritas: *Proc. Powder Metall. Congr. Exhib.*, Orlando, Florida, USA, 2002, pp. 53–62.
10. Y.C. Peng, H.J. Jin, J.H. Liu, and G.L. Li: *Mater. Sci. Eng. A*, 2011, vol. 529, pp. 321–25.
11. H.O. Gulsoy, M.K. Bilici, Y. Bozkurt, and S. Salman: *Mater. Des.*, 2007, vol. 28, pp. 2255–59.
12. J. Lentz, A. Röttger, and W. Theisen: *Acta Mater.*, 2015, vol. 99, pp. 119–29.
13. C. Yang, F. Liu, G. Yang, Y. Chen, N. Liu, and Y. Zhou: *J. Alloys Compd.*, 2007, vol. 441, pp. 101–06.
14. Y. Tomita: *Int. Mater. Rev.*, 2000, vol. 45, pp. 27–37.
15. H. Fayazfar, M. Salarian, A. Rogalsky, D. Sarker, P. Russo, V. Paserin, and E. Toyserkani: *Mater. Des.*, 2018, vol. 144, pp. 98–128.
16. Z. Xiu, A. Salwen, X. Qin, F. He, and X. Sun: *Powder Metall.*, 2003, vol. 46, pp. 171–74.
17. M.W. Wu, Y.C. Fan, H.Y. Huang, and W.Z. Cai: *Metall. Mater. Trans. A*, 2015, vol. 46A, pp. 5285–95.
18. T.B. Sercombe: *Mater. Sci. Eng. A*, 2003, vol. 344, pp. 312–17.
19. M. Sarasola, T. Gómez-Acebo, and F. Castro: *Acta Mater.*, 2004, vol. 52, pp. 4614–22.
20. R. Annamalai, A. Upadhyaya, and D. Agrawal: *Bull. Mater. Sci.*, 2013, vol. 36, pp. 447–56.
21. F.L. Serafini, M. Peruzzo, I. Krindges, M.F.C. Ordoñez, D. Rodrigues, R.M. Souza, and M.C.M. Farias: *Mater. Charact.*, 2019, vol. 152, pp. 253–64.
22. S. Ma, J. Xing, S. Guo, Y. Bai, H. Fu, P. Lyu, Z. Huang, and W. Chen: *Mater. Chem. Phys.*, 2017, vol. 199, pp. 356–69.
23. M. Selecka, A. Salak, L. Parilak, and H. Danninger: *Proc. 2000 PM World Congr.*, Kyoto, Japan, JPMA ed., 2000, Part 1, pp. 16–20.
24. T. Ogawa and T. Koseki: *Weld. Res. Suppl.*, 1989, vol. 68, pp. 181–91.
25. M. Selecká, A. Šalak, and H. Danninger: *J. Mater. Process. Technol.*, 2003, vol. 143, pp. 910–15.
26. X. Wei, Z. Chen, J. Zhong, L. Wang, W. Yang, and Y. Wang: *Comput. Mater. Sci.*, 2018, vol. 147, pp. 322–30.
27. M. Sarasola, S. Sainz, and F. Castro: *Euro. PM Conf. Proc.*, 2005, vol. 1, pp. 349–56.
28. C. Tojal, T. Gómez-Acebo, and F. Castro: *Mater. Sci. Forum*, 2007, vols. 534–536, pp. 661–64.
29. M. Skaloň, M. Hebdá, K. Sulikowska, and J. Kazior: *Mater. Des.*, 2016, vol. 108, pp. 462–69.
30. M.V. Sundaram, K.B. Surreddi, E. Hryha, A. Veiga, S. Berg, F. Castro, and L. Nyborg: *Metall. Mater. Trans. A*, 2018, vol. 49A, pp. 255–63.
31. M.W. Wu, W.Z. Cai, Z. Lin, and S. Chang: *Mater. Des.*, 2017, vol. 133, pp. 536–48.
32. M.W. Wu and W.Z. Cai: *Mater. Charact.*, 2016, vol. 113, pp. 90–97.
33. S. Egashira, T. Sekiya, T. Ueno, and M. Fujii: *Jpn Soc. Mech. Eng.*, 2019, vol. 6, pp. 1–11.
34. B.H. Rabin and R.M. German: *Metall. Trans. A*, 1988, vol. 19, pp. 1523–32.
35. H.I. Bakan, D. Heaney, and R.M. German: *Powder Metall.*, 2001, vol. 44, pp. 235–42.
36. Z. Liu, X. Chen, Y. Li, and K. Hu: *J. Iron Steel Res. Int.*, 2009, vol. 16, pp. 37–42.
37. H. Fu, Q. Xiao, J. Kuang, and J. Xing: *Mater. Sci. Eng. A*, 2017, vol. 466, pp. 160–65.
38. F. Li and Z. Li: *J. Alloys Compd.*, 2014, vol. 587, pp. 267–72.
39. J.O. Andersson, T. Helander, L. Hoglund, P. Shi, and B. Sundman: *CALPHAD*, 2002, vol. 26, pp. 273–312.
40. Y. Yi, Q. Li, J. Xing, H. Fu, D. Yi, Y. Liu, and B. Zheng: *Mater. Sci. Eng. A*, 2019, vol. 754, pp. 129–39.
41. N. Tosangthum, P. Kunnam, M. Morakotjinda, W. Koetniyom, R. Krataitong, P. Wila, and R. Tongsrri: *Key Eng. Mater.*, 2019, vol. 798, pp. 9–16.
42. J. Karwan-Baczewska: *Arch. Metall. Mater.*, 2011, vol. 56, pp. 789–96.
43. W. Koetniyom, P. Chantawet, N. Tosangthum, M. Morakotjinda, T. Yotkaew, P. Wila, and R. Tongsrri: *J. Met. Mater. Miner.*, 2019, vol. 29, pp. 22–30.
44. R.M. German and K.A. D’Angelo: *Int. Met. Rev.*, 1984, vol. 29, pp. 229–72.
45. P. Sang, H. Fu, Y. Qu, C. Wang, and Y. Lei: *Werkstofftech*, 2015, vol. 46, pp. 962–69.
46. X. Ren, H. Fu, J. Xing, Y. Yang, and S. Tang: *J. Mater. Res.*, 2017, vol. 32, pp. 3078–88.
47. Y. Penghui, F. Hanguang, L. Guolu, L. Jinhai, and Z. Xuebo: *Mater. Des.*, 2020, vol. 186, p. 108363.
48. M.A. Taha, A.F. Yousef, K.A. Gany, and H.A. Sabour: *Mat.-wiss. u. Werkstofftech*, 2012, vol. 43, pp. 913–23.

**Publisher’s Note** Springer Nature remains neutral with regard to jurisdictional claims in published maps and institutional affiliations.